

Journal of Materials Chemistry A

Accepted Manuscript



This is an *Accepted Manuscript*, which has been through the Royal Society of Chemistry peer review process and has been accepted for publication.

Accepted Manuscripts are published online shortly after acceptance, before technical editing, formatting and proof reading. Using this free service, authors can make their results available to the community, in citable form, before we publish the edited article. We will replace this *Accepted Manuscript* with the edited and formatted *Advance Article* as soon as it is available.

You can find more information about *Accepted Manuscripts* in the [Information for Authors](#).

Please note that technical editing may introduce minor changes to the text and/or graphics, which may alter content. The journal's standard [Terms & Conditions](#) and the [Ethical guidelines](#) still apply. In no event shall the Royal Society of Chemistry be held responsible for any errors or omissions in this *Accepted Manuscript* or any consequences arising from the use of any information it contains.

Cite this: DOI: 10.1039/c0xx00000x

www.rsc.org/xxxxxx

ARTICLE TYPE

N-doped Carbon Foam Based Three-dimensional Electrode Architectures and Asymmetric Supercapacitors

Jie Wang, Laifa Shen, Ping Nie, Xiaoliang Yun, Yunling Xu, Hui Dou and Xiaogang Zhang*

Received (in XXX, XXX) Xth XXXXXXXXX 200X, Accepted Xth XXXXXXXXX 200X

DOI: 10.1039/b000000x

Improving the electrochemical performance of supercapacitors mainly depend on electrode design and system construction. A new kind of additive-free asymmetric supercapacitors (ASCs) has been successfully fabricated with self-supported carbon foam/ordered mesoporous carbon film (CF-OMC) as negative electrode and free-standing CF-NiCo₂O₄ nanosheets (NS) as positive electrode, respectively. 10 highly conductive three-dimensional (3D) CF framework could facilitate electron transfer while the porous thin film of OMC and ultrathin NiCo₂O₄ nanosheets could shorten the ion diffusion paths and facilitate the rapid migration of electrolyte ions. The optimized asymmetric supercapacitors could work reversibly in 0-1.6 V, delivering a high energy density (~47.8 Wh kg⁻¹), high power density (~9800 W kg⁻¹ at 17.7 Wh kg⁻¹) and outstanding cycle stability (~10 000 times). This research may pave the way 15 for fabricating lightweight, low-cost, and high-performance electrode for energy storage applications.

1. Introduction

The exponential growth of the market for portable electronic devices has created an ever-increasing demand for light-weight electric power sources of high energy and power density. 20 Electrochemical capacitors (ECs),^{1, 2} also called supercapacitors or ultracapacitors, have been widely used in portable electronics, back-up power sources and electrical vehicles due to their high power density, fast delivery rate, and long life span.^{3, 4} However, commercial supercapacitors suffer from a low energy density, 25 which has restricted their potential applications. A major effort has been directed toward maximizing the device capacitance (C) and/or the operating voltage (V) since the amount of electrical energy (E) accumulated in a capacitor is proportional to CV.⁵

$$E = 1/2CV^2 \quad (1)$$

30 Traditionally asymmetric supercapacitors (ASCs) consist of a battery-type and a capacitor-type electrode, which can make full use of the high energy density of faradic electrode and high power density of electrochemical double-layer (EDL) electrode in the same electrolyte. More importantly, this design is an effective 35 approach for extending the operation voltage and notably improving the energy density.⁶⁻⁸ The negative materials for ASCs mainly consist of porous carbon, while oxides and polymers often act as positive electrode materials.⁶⁻⁹ To significantly improve the capacitive performance of electrodes, the design of the 40 microstructure of electrode materials in a way they can be utilized to a fuller extent is the key. A promising approach to this end is to engineer electrodes with high specific surface area (SSA) and optimized hierarchical nanostructures.¹⁰⁻¹⁴ So far an intense research effort has been devoted to architecture design of

45 nanomaterials for ASCs to improve the power capabilities and life cycles. Among the numerous nanostructures, two dimensional (2D) nanosheets (NS) are the most attractive because of the high interfacial areas and short diffusion path lengths, which consequently improves the effective electrochemical 50 utilization and favors electrolyte ions migration.^{13, 15, 16} In addition, the combination of 2D NS with three dimensional (3D) conductive substrates, as binder-free electrode materials, can further facilitate the electron transfer and are more desirable for future electronics.¹⁷⁻¹⁹ Therefore, it will be of great significance to 55 develop some effective and facile methods to grow mesoporous nanoarrays directly on the conductive substrates for high energy density supercapacitors.

Ternary nickel cobaltite (NiCo₂O₄) has recently been investigated a lot because of its much higher electrical 60 conductivity and electrochemical activity compared to binary nickel oxide (NiO) and cobalt oxide (Co₃O₄).²⁰⁻²⁴ More importantly, being cost effective and available in various morphologies make NiCo₂O₄ an attractive candidate for electrode material. Over the past few years, considerable scientific 65 endeavors have been directed on *in situ* growing NiCo₂O₄ NS on conductive substrate. For instance, Zhang and co-workers synthesized hierarchical nanostructured NiCo₂O₄ thin films onto three-dimensional nickel foam scaffold as a high-performance electrode for electrochemical capacitors.²² Yu et al. reported a 70 flexible pseudocapacitive electrode by coating mesoporous NiCo₂O₄ nanoarrays on flexible carbon cloth.²⁴ In this regard, 2D NS grown on the conductive substrates can not only provide a large electrode surface area and good conductivity, but also endure the large volume changes. However, considering the 75 weight of the substrates and low loading mass of active materials, the gravimetric capacitance with respect to the total mass of the

electrode has been very low.

The vast majority of negative electrode materials are high surface area activated carbon and related materials.⁶⁻⁹ But these carbon materials generally lack well-defined mesopores and/or micropores, substantially limiting the efficiency of mass transport and charge storage. Considering the electrode kinetic mechanisms and the correlation between porous structure of carbons and electrolyte ions, it is highly attractive to build up hierarchical porous architectures by integrating small mesoporous channels within interconnected macroporous frameworks to strengthen the EDL capacitance.²⁵⁻²⁷ Thus, it is attractive to develop a simple and cost-effective approach to design freestanding carbon materials with high surface area and appropriate porosity structure as EC electrodes. Recently, a new kind of carbon nanofoam paper prepared by infiltrating low-density carbon fiber papers with phenolic resin is reported. The obtained composites with 3D interconnected network of mesopores and macropores exhibits high flexibility and electronic conductivity as electrode material.²⁸

Melamine foam (MF) is a low-cost commercially available polymer foam, mainly composed of formaldehyde-melamine resin.²⁹ By direct carbonization, a novel nitrogen-doped carbon foam (CF) with a low density (5 mg cm^{-3}) and highly electrical conductive 3D elastic interconnected network could be prepared. These properties make CF a promising candidate to provide flexible and free-standing 3D conductive framework, serving as robust 3D highly conductive matrix for constructing hierarchical porous structure and for accommodating other electrochemically active materials.^{30, 31} In this work, we construct an ASC containing 3D CF-ordered mesoporous carbon films (OMC), derived from assemble of MF and resol, as negative electrode, and CF-coated NiCo_2O_4 prepared through hydrothermal reaction as positive electrode. In our approach, first we focus on the design of binder-free electrode which enhances the ion diffusion as well as electron transport at the electrode/electrolyte interface. In addition, the hierarchical nanostructured electrode material with mesoporous nanoarrays and 3D conductive framework, which effectively improves electro-active surface area, is another point to be emphasized. The optimized device can operate stably up to 1.6 V with a specific capacitance of 134 F g^{-1} , reaching an energy density of 47.8 Wh kg^{-1} at a power density of 640 W kg^{-1} . Meanwhile, such ASCs exhibit good cycling durability with 91% specific capacitance retained after 10000 cycles.

2. Experimental

2.1. Materials Synthesis

Preparation of CF: MFs were obtained from SINOYQX (Sichuan, China). The MFs were put into an electric furnace and heated in nitrogen at $350 \text{ }^\circ\text{C}$ for 2 h with a heating rate of $1 \text{ }^\circ\text{C min}^{-1}$, which was followed by further treatment at $900 \text{ }^\circ\text{C}$ for 2 h with a heating rate of $5 \text{ }^\circ\text{C min}^{-1}$. The as-prepared CF was taken out after the temperature was cooled down to below $80 \text{ }^\circ\text{C}$.

Preparation of CF-OMC: A 50 wt% phenol-formaldehyde (PF) resol solution in ethanol (pH=7) was first synthesized according to an established method.^[25] In a typical synthesis, 1.0 g PF sol was mixed with 0.25 g F127 and stirred for at least 6 h at room temperature to form a homogeneous, yellow solution. MF

monoliths (4 g) were infiltrated with the above precursor solution inside a capped container and then placed in a vacuum oven for 3–6 h at $30\text{--}50 \text{ }^\circ\text{C}$ to remove the solvent. This procedure was repeated several times to ensure no excess solution left. Cross-linking was achieved by thermally curing the precursor-infiltrated monoliths at $100 \text{ }^\circ\text{C}$ for 24 h. CF-OMC monoliths were obtained through pyrolysis in nitrogen at $350 \text{ }^\circ\text{C}$ for 2 h at a heating rate of $1 \text{ }^\circ\text{C min}^{-1}$ to remove F127, and then rising to $900 \text{ }^\circ\text{C}$ at $5 \text{ }^\circ\text{C min}^{-1}$ for 2 h for further carbonization. The mass ratio of CF and OMC in the final product is estimated to be 1:1. For comparison, 0.5 g PF sol was used in this process to prepare a product CF-OMC0.5 (the mass ratio of CF and OMC is 2:1).

Growth NiCo_2O_4 NS on CF: NiCo_2O_4 NS grown on CF by a hydrothermal method reported by Lou's group with minor modifications.^[23] 0.5 mmol of $\text{Ni}(\text{NO}_3)_2 \cdot 6\text{H}_2\text{O}$, 1 mmol of $\text{Co}(\text{NO}_3)_2 \cdot 6\text{H}_2\text{O}$ and 2.2 mmol of hexamethylenetetramine are dissolved into 20 mL of water to form a transparent pink solution. The obtained CF was fully immersed into the above solution and then transferred to a Teflon-lined stainless steel autoclave and kept at $90 \text{ }^\circ\text{C}$ for 6 h. After hydrothermal growth, the CF covered with NiCo-precursor NSs was carefully rinsed several times with de-ionized water and absolute ethanol, and finally dried in air. Then, the sample was calcined at $300 \text{ }^\circ\text{C}$ for 2 h to get well defined crystallized NiCo_2O_4 NSs on CF. In average, the mass percentage of NiCo_2O_4 in the final composite is estimated to be 28 %, carefully weighted after calcination.

2.2. Materials Characterization

Field emission scanning electron microscopy (FESEM) and transmission electron microscopy (TEM) were carried out with a JEOL JSM-6380LV FESEM and JEOL JEM-2010, respectively. Powder X-ray diffractions (XRD) was studied by Bruker D8 Advance X-ray diffractometer using $\text{Cu K}\alpha$ radiation. The X-ray photoelectron spectroscopy (XPS) analysis was performed on a Perkin-Elmer PHI 550 spectrometer with $\text{Al K}\alpha$ (1486.6 eV) as the X-ray source. The nitrogen (N_2) adsorption-desorption isotherms of the samples were conducted by using a Micromeritics BK122T-B analyzer. The SSA was determined according to the BET theory in the relative pressure range from 0.04 to 0.2. The total pore volumes were the adsorbed amount at a P/P_0 of 0.992. The pore size distributions (PSD) were derived from the adsorption branches of isotherms using the Barrett-Joyner-Halenda (BJH) model.

2.3. Electrochemical Measurements

All the electrochemical measurements were carried out on a CHI 660D electrochemical workstation in the 6 M KOH aqueous solution. Three-electrode systems were used to measure the response of the CF-OMC and CF- NiCo_2O_4 composite as the working electrode, with a Pt foil as the counter electrode and a saturated calomel electrode (SCE) as the reference electrode, respectively. The asymmetric supercapacitor was measured with a two-electrode system, where CF-OMC composite was the negative electrode and the CF- NiCo_2O_4 composite was the positive electrode. In our experiments, both CF-OMC and CF- NiCo_2O_4 composites were pressed with 10 Mpa force and in this way the volume was significantly decreased. The two electrodes and a PTFE separator permeable to ion transport were placed into a test fixture consisting of two stainless steel plates. All the

operating current densities were calculated based on the mass of active materials (CF-OMC and NiCo₂O₄ for the 3-electrode system and the total weight of CF-OMC and NiCo₂O₄ for the 2-electrode system). The gravimetric specific capacitance for the three-electrode cell was obtained from the galvanostatic charge/discharge curves as:

$$C_{\text{single}} = I \cdot t / m_s \cdot V, \quad (2)$$

where m_s (g) is the mass of active materials, I (A) is the current density, t (s) is the discharge time and V (V) is the discharge voltage range.

For the two electrode system, the mass ratio between the positive and negative electrode is obtained based on the following equation:

$$m_+ / m_- = C_- \cdot V_- / C_+ \cdot V_+, \quad (3)$$

and the gravimetric specific capacitance is obtained by the equation:

$$C_{\text{single}} = 4I \cdot t / m \cdot V, \quad (4)$$

where m is the total mass of active materials.

The energy density is calculated as:

$$E = C_{\text{single}} \cdot V_{\text{max}}^2 / 2, \quad (5)$$

while the power density is calculated by the equation:

$$P = E / t \quad (6)$$

3. Results and discussions

3.1 Carbon foam/ordered mesoporous carbon

The synthesis route of CF-OMC foam is described in Figure 1. Firstly, MF is immersed in the sol containing resin/surfactant precursors in ethanol solution, and the organic-organic self-assembly of the resins and Pluronic F127 triblock copolymers occurs during the evaporation of ethanol at room temperature (EISA process). The as-obtained foam is heated under an inert atmosphere to decompose the triblock copolymers at 350 °C, while the phenolic resin and MF are carbonized at 900 °C. Through this route, free-standing 3D CF-OMC foam with hierarchically porous structure has been successfully synthesized.



Figure 1. Scheme for preparation of CF-OMC.

The precursor MF is a commercially available polymer foam with a 3D elastic interconnected framework (Figure S1, see Supporting Information). After calcination, SEM image in Figure 2a reveals that the as-prepared CF inherits concave triangle fiber shape of the precursor and builds a cellular structure with pore diameters of about 20-50 μm. For CF-OMC, clearly shown in Figure 2b and c, thin membranes with a slight curvature can be observed intercrossed with the adjacent struts. From the fracture edge (Figure 2d), the thickness of carbon nanosheets is estimated to be 20-30 nm. TEM characterization (Figure 2e and 2f) revealed that the mesopores in the OMC film are open, parallel 1D channels with a uniform size.

The N₂ adsorption-desorption isotherms and PSD of CF-OMC were further examined (Figure 3a). A typical type-IV curve (in the IUPAC classification) with a clear H₁-type hysteresis loop in a relative pressure range of 0.4–0.7 is observed for CF-OMC, implying a narrow distribution of the mesoporous characteristics.³² The BJH PSD curve from adsorption branches is shown in Figure 3b. The average mesopore size of CF-OMC is ~3.1 nm. Furthermore, the SSA and the pore volume (PV) are calculated to be as high as 939.97 m² g⁻¹ and 0.41 cm³ g⁻¹. In comparison, the pure CF and CF-OMC0.5 show lower SSAs of 195 and 451 m² g⁻¹ (Figure S2). Accordingly, the BET surface area of CF-OMC mainly comes from the mesopores of the OMC membranes. In addition, the SSA of the reported OMC

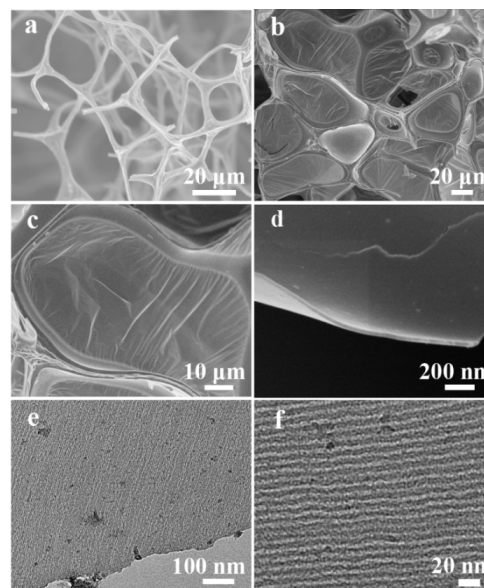


Figure 2. FE-SEM images of pure CF (a) and CF-OMC (c-d). TEM images of OMC films scratched from CF-OMC (e and f).

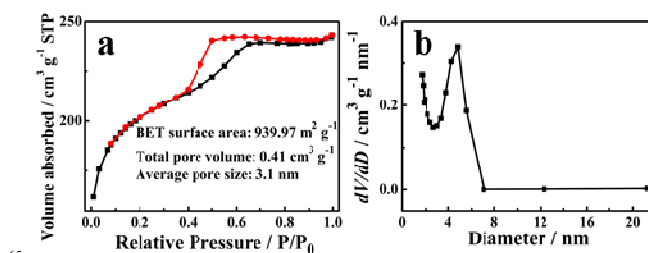


Figure 3. (a) N₂ adsorption-desorption isotherms and (b) PSD curve of CF-OMC.

powder prepared by resol and F127 is $690 \text{ m}^2 \text{ g}^{-1}$, which is far below the SSA normalized to the OMC films in the CF-OMC composite. Therefore CF is demonstrated to play a critical role as supporting scaffold for providing large space to accommodate resol and promoting formation of carbon films.

To evaluate the chemical composition, nature of bonding, and purity of CF-OMC, XPS measurement was carried out. The XPS survey spectra shown in Figure 4a demonstrates the presence of C, N and O. The C, N and O content determined from XPS spectra, expressed in at.%, was about 75, 6.7 and 18.3 %, respectively. From the C1s spectrum (Figure 4b), the most pronounced peak located at 284.6 eV (C-I) is characteristic of carbon lattice, and the rest peaks are C–N (C-II), C–O (C-III) and C=O (C-IV) in sequence.³³ The deconvolutions of the N 1s region spectrum to identify the surface functionalities are shown in Figure 4c and fitted by four component peaks, which are attributed to quaternary (N-Q), pyrrolic (N-5), pyridinic nitrogen (N-6) and oxidized pyridinic nitrogen (N-X), respectively.^{34, 35} During carbonization, the MF decomposes and produces NH_3 , which may dope the OMC film. The existence of nitrogen can be attributed to both the CF and OMC (Figure S3). The high-resolution O1s spectrum in Figure 4d clearly reveals the existence of several oxygen-based groups including C=O quinone type groups (O-I), and C–OH phenol groups (O-II) and/or C–O–C ether groups (O-III).³⁶ The existence of surface functionalities are very important for the application of supercapacitors since they can not only improve the wettability but also undergo fast redox reaction in aqueous electrolytes, giving rise to a pseudo-capacitive contribution.

The above characterization results demonstrate the unique features of CF-OMC, including abundant porous structure, short diffusion paths, high electrically conductive networks and good wettability. To evaluate the advantages of CF-OMC, the electrochemical performance was first measured by using a three-electrode system in electrolyte of 6 M KOH. CV curves obtained at different scan rates with CF-OMC composite are shown in Figure 5a and b. From 5 to 50 mV s^{-1} , the curves present the typical “rectangular shape” expected for an ideal capacitor. At higher scan rates, even at 500 mV s^{-1} , the shape of the curve is still satisfactory, which indicates quick dynamics of charge propagation with this kind of material.

The galvanostatic charge/discharge (GC) curves presented in Figure 5c for five values of the loading current show isosceles triangular shapes. This confirms that capacitors based on this composite can be loaded to a high regime while retaining good capacitive behavior. The specific capacitance calculated from the charge discharge curve is $\sim 203 \text{ F g}^{-1}$ at a current density of 0.5 A g^{-1} . The capacitance retention ratio of CF-OMC with a slight decrease at various charge/discharge current densities is shown in Figure 5d. When the current density is increased to 20 A g^{-1} , it exhibits a specific capacitance of 132 F g^{-1} and maintains 64.8 % compared to the initial capacitance. The electrochemical performance of pure CF is demonstrated in Figure S4. The CF electrode exhibits a distorted CV profile even at a scan rate of 200 mV s^{-1} . The specific capacitance of CF calculated from GC is $\sim 150 \text{ F g}^{-1}$ and the capacitance of OMC films in CF-OMC could be deduced to be 240 F g^{-1} . It is verified that either values of CF-OMC or OMC films are much higher than those for resol derived

OMC in the form of granular powders, particularly at high scan rates and high current densities.^{37, 38}

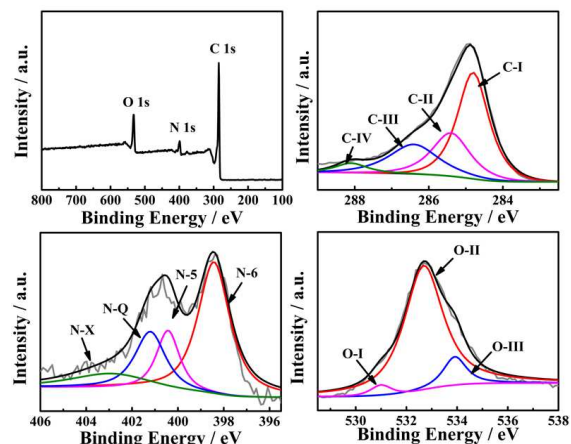


Figure 4. XPS results for CF-OMC: (a) survey scan, (b) C 1s, (c) N 1s, and (d) O 1s spectra.

Electrochemical impedance spectroscopy (EIS) is carried out to prove that the short diffusion path of CF-OMC for electrolyte ions enhances ion transport kinetics. The resulting Nyquist plots exhibit inconspicuous Warburg curve, reflecting the short ion diffusion path in the electrode.³⁹ At low frequencies, the nearly vertical behavior indicates that the surface area of the internal structure of the porous carbon electrode is wetted by the electrolytes. Moreover, the cycle life is an important requirement for supercapacitors and the capacitance retention as a function of cycle number is shown for CF-OMC in Figure 5f. Even after charging-discharging for 10 000 cycles at a current density of 1 A g^{-1} , the capacitive retention is still as high as 96 %.

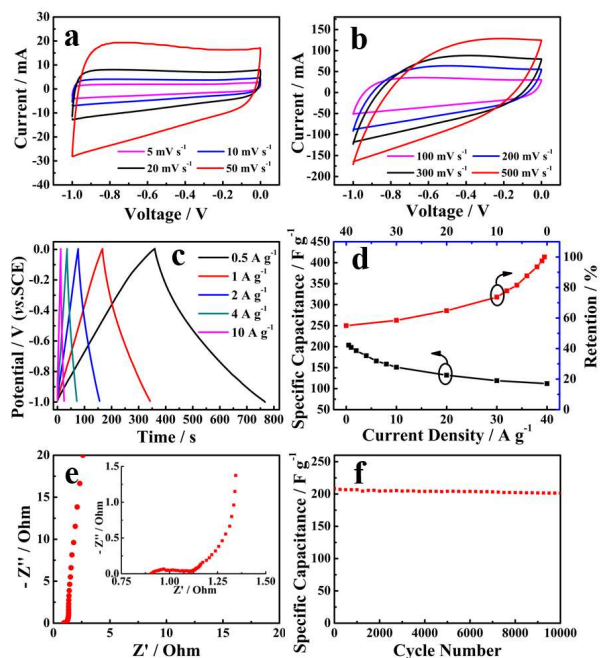


Figure 5. Electrochemical performance of CF-OMC: (a and b) CV curves at different scan rates. (c) GC curves at different current densities. (d) Specific capacitance and its retention ratio at different current densities. (e) Nyquist plots with a magnification for the high-frequency region in the inset. (f) Cycle life test at a current density of 1.0 A g^{-1} .

The excellent performance of CF-OMC for supercapacitor should be ascribed to the highly conductive CF and the structural/textural advantage: firstly, the highly conductive CF with continuous framework could facilitate electron transport; secondly, the thin thickness of OMC films shortens the distance of electrolyte ion diffusion; the abundant opened mesopores favors the access of ions to the active surface while the micropores strengthen the EDL capacitance. In addition, the abundant heteroatoms could introduce some pseudocapacitance through reversible redox reactions. These results suggest the possibility and superiority of fabricating nano devices based on free-standing CF-OMC composite for electrochemical applications.

3.2 Carbon foam/NiCo₂O₄ nanosheets

The structure of the CF-NiCo₂O₄ composite was studied by XRD. All the diffraction peaks of the CF-NiCo₂O₄ are either due to carbon or NiCo₂O₄. The seven well-defined diffraction peaks are observed at 2θ values of 18.9°, 31.1°, 36.6°, 44.6°, 59.1°, 64.9° and 68.3°. All of these peaks can be successfully indexed to (111), (220), (311), (400), (511), (440) and (531) plane reflections of the spinel NiCo₂O₄ crystalline structure (JCPDF: 20-0781), with the standard peaks indicated in Figure 6a. XPS was used to identify the presence and oxidation state of the as-synthesized NiCo₂O₄ covering CF. A full-survey-scan spectrum in Figure 6b indicates the presence of Ni, Co, O, as well as C elements and the absence of other impurities. By using a Gaussian fitting method, the Ni 2p was also fitted with two spin-orbit doublets, characteristic of Ni²⁺ and Ni³⁺, and two shakeup satellites (Figure 6c).⁴⁰ The Co 2p emission spectrum (Figure 6d) was best fitted with two spin-orbit doublets, characteristic of Co²⁺ and Co³⁺, and one shakeup satellite (indicated as "Sat."). These results show that the chemical composition of mesoporous NiCo₂O₄ nanowires contain Co²⁺, Co³⁺, Ni²⁺, and Ni³⁺, which are in good agreement with the results in the literature for NiCo₂O₄.

Detailed structural information was further obtained using SEM and TEM. From a typical SEM image (Figure 7a), it is clear that the as-synthesized CF-NiCo₂O₄ composites demonstrate an

attractive hierarchical nanostructure. It can be seen that large-scale, dense and aligned NiCo₂O₄ nanosheets grow uniformly on the entire skeleton of the CF. The NiCo₂O₄ nanosheets appear like numerous "leaves", standing perpendicularly on the CF substrate. A careful examination (Figure 7b) reveals that these sheet-like NiCo₂O₄ are 0.5-1 μm in diameter and about 5-10 nm in thickness at the middle section. The interconnected structure offers outstanding advantages in enhancing ionic and electronic conductivity of pseudocapacitive NiCo₂O₄. The pores or voids between the nanosheets not only allow rapid ion transport but also provide a large specific interface between NiCo₂O₄ and electrolytes, facilitating the full realization of the pseudocapacitance of NiCo₂O₄. Some NiCo₂O₄ particles were observed in the same reaction batch but were not attached to the CF, and they also composed of nanoflakes with roughly spherical morphology (Figure S5). More detailed structural information of the NiCo₂O₄ nanosheets were investigated by TEM. The low-magnification image (Figure 7c) indicates that the nanosheets are continuous with a smooth surface. From the HRTEM image of Figure 7d, the measured lattice spacing of 0.25 nm and 0.2 nm is corresponding to the (311) and (400) planes of cubic NiCo₂O₄, respectively. The porous textures of NiCo₂O₄/CF were analyzed by N₂ sorption measurement (Figure S6). The BET SSA, average pore size and mesopore volume of the NiCo₂O₄/CF were quantitatively summarized as 96 m² g⁻¹, 2.1 nm and 0.58 cm³ g⁻¹, respectively.

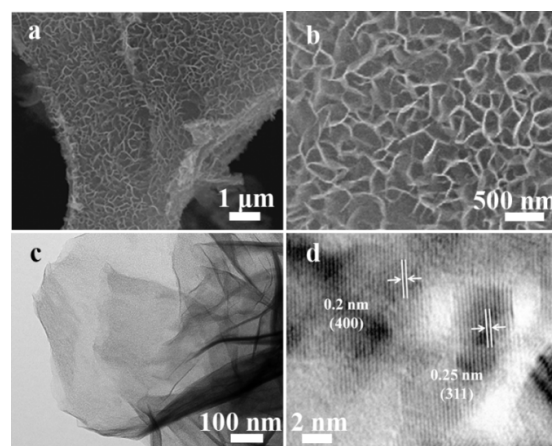


Figure 7. (a, b) SEM images of the CF-NiCo₂O₄ composite, showing all nanosheets completely surrounding CF. (c) TEM and (d) HRTEM images of NiCo₂O₄ NS scratched down from the CF.

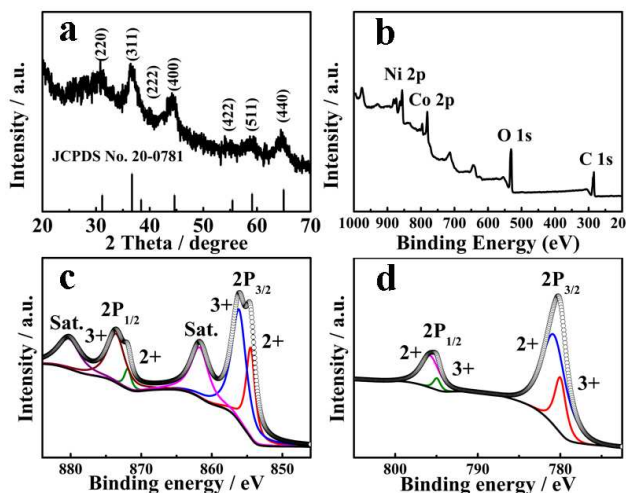


Figure 6. (a) XRD pattern of the CF-NiCo₂O₄ composite. (b) XPS survey spectra of NiCo₂O₄ NS. High-resolution XPS spectra of (c) Ni 2p and (d) Co 2p for the ultrathin mesoporous NS.

To evaluate the capacitive performance of the binder-free CF-NiCo₂O₄ electrodes, CV and GC measurements were carried out in 6 M KOH. Figure 8a shows CV curves of the CF-NiCo₂O₄ with various sweep rates ranging from 10 to 200 mV s⁻¹. A pair of oxidation and reduction peaks can be seen, which are related to the reversible Faradaic redox reaction of M-O/M-O-OH (M refers to Ni or Co).⁴¹ The high-power characteristic of the unique electrode can be identified from their voltammetric response at various scan rates. Apparently, all curves exhibit a similar shape, and the current increases with the increasing scan rate. Even at a scan rate of 200 mV s⁻¹, the CV curve still shows a pair of redox peaks, indicating that this hybrid structure is beneficial to fast redox reactions. The nonlinear charge/discharge curves (Figure 8b) further verified the pseudo-capacitance behavior. The

gravimetric capacitance of the active materials at various current densities is calculated from the discharge curves and is illustrated in Figure 8c (In this test condition, CF makes little contribution to capacitive (Figure S7)). It can be seen that the specific capacitance based on the mass of NiCo₂O₄ was 1140 F g⁻¹ at a current density of 1 A g⁻¹. The capacitance in this work is relatively lower than NiCo₂O₄ grown on other substrate.^{20, 42} However, it should be noted that the loading mass of active materials on the substrate in this work (more than 2.4 mg cm⁻²) is much higher than many other reports (usually less than 1 mg cm⁻²). In addition, the CF/NiCo₂O₄ exhibits good rate capability and superior cyclic stability. When the current density was increased to 20 A g⁻¹, the gravimetric capacitance can still retain 880 F g⁻¹ (77 % retention). The long-term cycling stability of the CF-NiCo₂O₄ composite was evaluated using a long-term galvanostatic charge/discharge process (Figure 8d). At the discharge current density of 4 A g⁻¹, the capacitance increased from 1028 F g⁻¹ to 1164 F g⁻¹ during the first 200 cycles, which may be attributed to the complete activation of NiCo₂O₄. After that, it gradually decreases to 946 F g⁻¹ after 3000 cycles, achieving capacitance retention of about 91 %. For binder enriched NiCo₂O₄ NS electrode, there is a significant change for the shape of CV curves and an obvious shift for the position of redox peak with the increase in sweep rate from 5 to 40 mV s⁻¹ (Figure S8a), suggesting that the electrode possesses large polarization. The specific capacitances of NiCo₂O₄ NS electrode are only 452 F g⁻¹ at 10 A g⁻¹, corresponding to around 63 % retention at 1 A g⁻¹ (Figure S8b and c).

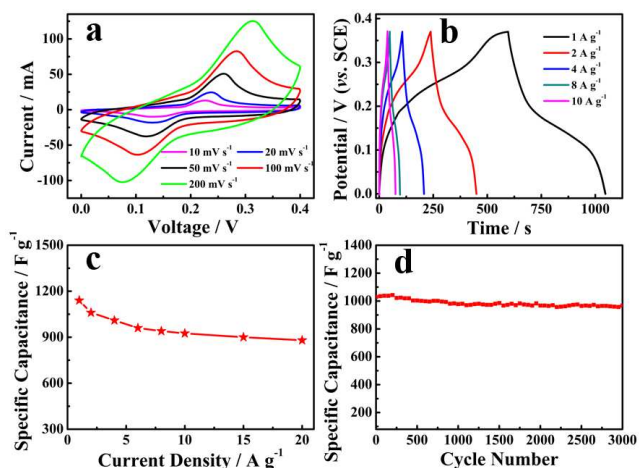


Figure 8. Electrochemical evaluations of the CF-NiCo₂O₄ composite: (a) CV curves at various scan rates. (b) Constant-current charge-discharge voltage profiles. (c) The corresponding specific capacitance as a function of current density. (d) Cycling performance at a current density of 4 A g⁻¹.

The observed ultra-high specific capacitance and excellent cyclic stability of the CF supported NiCo₂O₄ may offer the following structural advantages for electrochemical activity: firstly, the ultrathin and mesoporous characteristics of the NS provide more electroactive sites for redox reaction and facilitate the fast intercalation and de-intercalation of active species; the open space between these ultrathin NS and the mesopores existing in the nanosheets ensure efficient contact between the surface of electroactive nanosheets and the electrolyte at high rates. Furthermore, the direct contact between CF and NiCo₂O₄

builds up an express path for fast electron transport, which ensures every NS participates in the ultrafast electrochemical reaction.

3.3 Asymmetric Supercapacitors

An asymmetric supercapacitor was fabricated using CF-OMC as negative electrode and CF-NiCo₂O₄ composite as positive electrode with 6 M KOH aqueous electrolyte. Based on the above analysis of the specific capacitance values and potential ranges found for CF-NiCo₂O₄ and CF-OMC composite, the mass ratio of the positive electrode to the negative electrode was fixed close to 0.36 based on the charge balance theory.⁴³ A series of CV measurements with increasing voltage windows were used to estimate the best operating potential of the asymmetric supercapacitor cell (Figure 9a). It can be clearly seen that when the operating potential window extends from 1.0 to 1.6 V, more faradic reactions occur and the specific capacitance greatly increases from 74 to 128 F g⁻¹. This means that the stored energy and delivered power could be significantly improved according to the equation 1. Whereas the overall performance of supercapacitor improves with increasing cell voltage, evolution of oxygen occur with higher operating potential to 1.8 V.⁴⁴ Thus voltage of 1.6 V is chosen as working voltage in the subsequent research.

Figure 9b exhibits the CV curves of an optimized asymmetric supercapacitor at various scan rates (ranging from 5 to 100 mV s⁻¹) measured under 1.6 V in 6 M KOH aqueous electrolyte. A combination of both pseudocapacitive and EDL types of capacitance was clearly observed at all scan rates and the peak current becomes larger with the increasing scan rate. The typical GC curves of our ASCs can be observed in Figure 9c and the discharge curve is nearly symmetric with its corresponding charging counterpart, further indicating its excellent electrochemical reversibility and good Coulombic efficiency. The calculated specific capacitances of the ASC device at 0.5, 1, 2, 4 and 10 A g⁻¹ are 134, 120, 101, 80 and 65 F g⁻¹. The specific capacitance of the full cell is mainly limited by that of the carbon-based cathode; nevertheless, it is enhanced by the higher pseudocapacitance of CF-NiCo₂O₄ electrode to about 3-fold larger than conventional AC-based symmetric capacitors. Long cycle life is a critical requirement for supercapacitor devices. The cycle life test for CF-OMC//CF-NiCo₂O₄ ASCs operated at 1.6 V was evaluated by using galvanostatic charge/discharge cycling at 1 A g⁻¹. The cycling stability is presented in Figure 9d and the ASCs exhibit an outstanding cycling stability with 91% capacity remaining after 10 000 continuous cycles. To investigate the reason for capacity decay after long-term cycling, we re-opened the cell which has been subjected to long cycle performance, and did TEM and XRD characterizations. The capacity decay is probably due to the following reasons. First, the positive CF-NiCo₂O₄ electrode was partially changed to ternary oxides or hydroxides due to the intensive reactions with the alkaline electrolyte, which decreases their energy storage capacity (Figure S9). Second, the morphology of the interconnected ternary nanosheets was altered or damaged by the fast and long term cycling tests (Figure S10). Third, the fast and long-term cycling tests may result in the delamination of NiCo₂O₄ from the CF substrate.

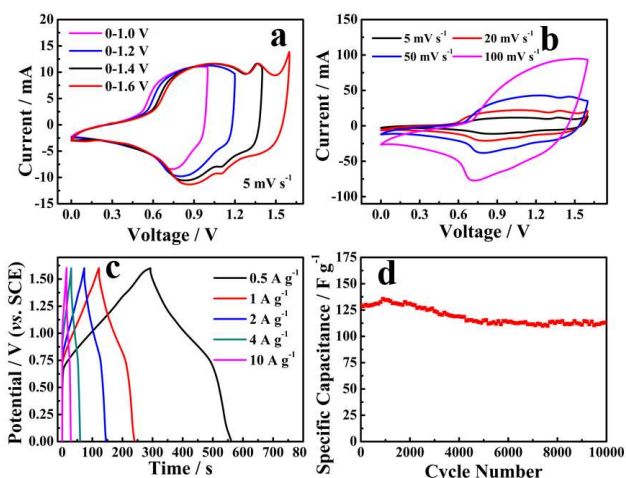


Figure 9. Electrochemical performance of CF-OMC//CF-NiCo₂O₄ based ASCs: (a) CV curves of measured at different potential window (at 5 mV s⁻¹). (b) CV curves at various scan rates. (c) Constant-current charge-discharge voltage profiles at different current densities. (d) Cycling performance at a current density of 1 A g⁻¹.

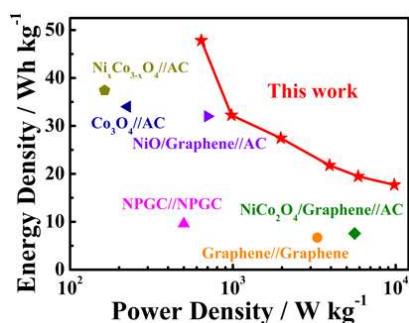


Figure 10. Ragone plot of CF-OMC//CF-NiCo₂O₄ based ASCs.

The power density and energy density calculated for the cells are shown in the Ragone plots (Figure 10). The CF-OMC//CF-NiCo₂O₄ asymmetric supercapacitor showed an energy density of 47.8 Wh kg⁻¹ at a power density of 640.1 W kg⁻¹, and a power density of 9.8 kW kg⁻¹ at an energy density of 17.69 Wh kg⁻¹. This high energy density is much higher than that of symmetrical supercapacitors, such as nitrogen-doped porous graphitic carbon (NPGC)//NPGC supercapacitors⁴⁵ and graphene//graphene supercapacitors⁴⁶ and some recently reported ASCs, such as binary metal oxides (NiCo₂O₄/graphene//AC, Ni_xCo_{3-x}O₄//AC) ASCs^{47, 48}, mono-metal oxide (NiO/graphene//AC, Co₃O₄//AC) ASCs^{49, 50}.

4. Conclusions

In summary, a high-performance ASCs based on hierarchical structured CF-OMC and CF-NiCo₂O₄ composite was first designed and fabricated via a facile and scalable method. This hierarchical architecture with 3D conductive network and 2D porous sheet facilitates fast ion diffusion and electron transfer at the electrode/electrolyte interface and also mitigates the structural destruction caused by ion insertion/deinsertion, leading to an outstanding electrochemical performance. The optimal device can be reversibly charged/discharged at an operation voltage of 1.6 V in 6.0 M KOH aqueous electrolyte, delivering a high energy density of 47.8 W h kg⁻¹ and a maximum power density of 9800

W kg⁻¹, possessing a remarkable cycling stability with approximately 91% capacity remaining after 10 000 cycles. These promising results demonstrate such a relatively easy-synthesis, low-cost, and macroscopic-scale electrode have great potential in the practical supercapacitor applications.

Acknowledgements

This work was supported by the National Basic Research Program of China (973 Program) (No. 2014CB239701), National Natural Science Foundation of China (No. 21173120, 21103091, 51372116), Natural Science Foundation of Jiangsu Province (BK2011030), the Fundamental Research Funds for the Central Universities of NUAA (NP2014403).

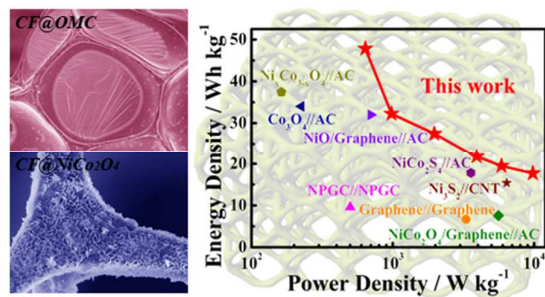
Notes and references

Jiangsu Key Laboratory of Material and Technology for Energy Conversion, College of Materials Science & Engineering, Nanjing University of Aeronautics and Astronautics, Nanjing, 210016, P.R. China.
Email: azhangxg@nuaa.edu.cn

1. A. S. Arico, P. Bruce, B. Scrosati, J.-M. Tarascon and W. van Schalkwijk, *Nat Mater*, 2005, **4**, 366-377.
2. Z. Yang, J. Zhang, M. C. W. Kintner-Meyer, X. Lu, D. Choi, J. P. Lemmon and J. Liu, *Chemical Reviews*, 2011, **111**, 3577-3613.
3. J. R. Miller and P. Simon, *Science*, 2008, **321**, 651-652.
4. J. Zhang and X. S. Zhao, *ChemSusChem*, 2012, **5**, 818-841.
5. P. J. Hall, M. Mirzaei, S. I. Fletcher, F. B. Sillars, A. J. R. Rennie, G. O. Shitta-Bey, G. Wilson, A. Cruden and R. Carter, *Energy & Environmental Science*, 2010, **3**, 1238-1251.
6. Y. G. Wang and Y. Y. Xia, *Electrochemistry Communications*, 2005, **7**, 1138-1142.
7. R. B. Rakhi, N. A. Alhebshi, D. H. Anjum and H. N. Alshareef, *Journal of Materials Chemistry A*, 2014, **2**, 16190-16198.
8. J. Yan, Z. Fan, W. Sun, G. Ning, T. Wei, Q. Zhang, R. Zhang, L. Zhi and F. Wei, *Advanced Functional Materials*, 2012, **22**, 2632-2641.
9. J. Zhang, J. Jiang, H. Li and X. S. Zhao, *Energy & Environmental Science*, 2011, **4**, 4009-4015.
10. G. Wang, L. Zhang and J. Zhang, *Chemical Society Reviews*, 2012, **41**, 797-828.
11. L. L. Zhang and X. S. Zhao, *Chemical Society Reviews*, 2009, **38**, 2520-2531.
12. Y. G. Wang and Y. Y. Xia, *Electrochimica Acta*, 2006, **51**, 3223-3227.
13. C. Yuan, X. Zhang, L. Su, B. Gao and L. Shen, *Journal of Materials Chemistry*, 2009, **19**, 5772-5777.
14. S. Xiong, C. Yuan, X. Zhang, B. Xi and Y. Qian, *Chemistry – A European Journal*, 2009, **15**, 5320-5326.
15. D. Puthusseri, V. Aravindan, S. Madhavi and S. Ogale, *Energy & Environmental Science*, 2014, **7**, 728-735.
16. H. Wang, H. S. Casalongue, Y. Liang and H. Dai, *Journal of the American Chemical Society*, 2010, **132**, 7472-7477.
17. N. A. Alhebshi, R. B. Rakhi and H. N. Alshareef, *Journal of Materials Chemistry A*, 2013, **1**, 14897-14903.

18. M. B. Sassin, C. N. Chervin, D. R. Rolison and J. W. Long, *Accounts of Chemical Research*, 2012, **46**, 1062-1074.
19. C. P. Rhodes, J. W. Long, K. A. Pettigrew, R. M. Stroud and D. R. Rolison, *Nanoscale*, 2011, **3**, 1731-1740.
20. C. Yuan, J. Li, L. Hou, X. Zhang, L. Shen and X. W. Lou, *Advanced Functional Materials*, 2012, **22**, 4592-4597.
21. G. Zhang and X. W. Lou, *Advanced Materials*, 2013, **25**, 976-979.
22. G. Q. Zhang, H. B. Wu, H. E. Hoster, M. B. Chan-Park and X. W. Lou, *Energy & Environmental Science*, 2012, **5**, 9453-9456.
23. G. Zhang and X. W. Lou, *Sci. Rep.*, 2013, **3**.
24. F. Deng, L. Yu, G. Cheng, T. Lin, M. Sun, F. Ye and Y. Li, *Journal of Power Sources*, 2014, **251**, 202-207.
25. J. Ji, L. L. Zhang, H. Ji, Y. Li, X. Zhao, X. Bai, X. Fan, F. Zhang and R. S. Ruoff, *ACS Nano*, 2013, **7**, 6237-6243.
26. W. Chen, R. B. Rakhi, M. N. Hedhili and H. N. Alshareef, *Journal of Materials Chemistry A*, 2014, **2**, 5236-5243.
27. H. J. Liu, W. J. Cui, L. H. Jin, C. X. Wang and Y. Y. Xia, *Journal of Materials Chemistry*, 2009, **19**, 3661-3667.
28. J. C. Lytle, J. M. Wallace, M. B. Sassin, A. J. Barrow, J. W. Long, J. L. Dysart, C. H. Renninger, M. P. Saunders, N. L. Brandell and D. R. Rolison, *Energy & Environmental Science*, 2011, **4**, 1913-1925.
29. S. Chen, G. He, H. Hu, S. Jin, Y. Zhou, Y. He, S. He, F. Zhao and H. Hou, *Energy & Environmental Science*, 2013, **6**, 2435-2439.
30. S. He and W. Chen, *Journal of Power Sources*, 2014, **262**, 391-400.
31. H. Hu, S. Liu, M. Hanif, S. Chen and H. Hou, *Journal of Power Sources*, 2014, **268**, 451-458.
32. Y. Tao, Tanaka, H. Tanaka, Ohkubo, T. Ohkubo, Kanoh, H. Kanoh, Kaneko and K. Kaneko, *Adsorption Science & Technology*, 2003, **21**, 199-203.
33. Y. Li, Y. Zhao, H. Cheng, Y. Hu, G. Shi, L. Dai and L. Qu, *Journal of the American Chemical Society*, 2011, **134**, 15-18.
34. L. F. Chen, X. D. Zhang, H. W. Liang, M. Kong, Q. F. Guan, P. Chen, Z. Y. Wu and S. H. Yu, *ACS Nano*, 2012, **6**, 7092-7102.
35. L. Qie, L. X. Yuan, W. X. Zhang, W. M. Chen and Y. H. Huang, *Journal of The Electrochemical Society*, 2012, **159**, A1624-A1629.
36. D. Hulicova-Jurcakova, M. Seredych, G. Q. Lu and T. J. Bandosz, *Advanced Functional Materials*, 2009, **19**, 438-447.
37. D. Feng, Y. Lv, Z. Wu, Y. Dou, L. Han, Z. Sun, Y. Xia, G. Zheng and D. Zhao, *Journal of the American Chemical Society*, 2011, **133**, 15148-15156.
38. X. Q. Zhang, Q. Sun, W. Dong, D. Li, A. H. Lu, J. Q. Mu and W. C. Li, *Journal of Materials Chemistry A*, 2013, **1**, 9449-9455.
39. Y. Wang, Z. Shi, Y. Huang, Y. Ma, C. Wang, M. Chen and Y. Chen, *The Journal of Physical Chemistry C*, 2009, **113**, 13103-13107.
40. B. Cui, H. Lin, Y. Z. Liu, J. B. Li, P. Sun, X. C. Zhao and C. J. Liu, *The Journal of Physical Chemistry C*, 2009, **113**, 14083-14087.
41. H. Wang, Q. Gao and L. Jiang, *Small*, 2011, **7**, 2454-2459.
42. Z. Wu, Y. Zhu and X. Ji, *Journal of Materials Chemistry A*, 2014, **2**, 14759-14772.
43. V. Khomenko, E. Raymundo-Piñero and F. Béguin, *Journal of Power Sources*, 2006, **153**, 183-190.
44. Z. S. Wu, W. Ren, D. W. Wang, F. Li, B. Liu and H. M. Cheng, *ACS Nano*, 2010, **4**, 5835-5842.
45. L. Sun, C. Tian, Y. Fu, Y. Yang, J. Yin, L. Wang and H. Fu, *Chemistry – A European Journal*, 2014, **20**, 564-574.
46. H. Wang, Y. Liang, T. Mirfakhrai, Z. Chen, H. Casalongue and H. Dai, *Nano Res.*, 2011, **4**, 729-736.
47. H. Wang, C. B. Holt, Z. Li, X. Tan, B. Amirkhiz, Z. Xu, B. Olsen, T. Stephenson and D. Mitlin, *Nano Res.*, 2012, **5**, 605-617.
48. X. Wang, C. Yan, A. Sumboja and P. S. Lee, *Nano Energy*, 2014, **3**, 119-126.
49. H. Wang, H. Yi, X. Chen and X. Wang, *Journal of Materials Chemistry A*, 2014, **2**, 3223-3230.
50. X. Zhang, Y. Zhao and C. Xu, *Nanoscale*, 2014, **6**, 3638-3646.

TOC



A high-performance asymmetric supercapacitor was constructed with self-supported carbon foam(CF)/ordered mesoporous carbon film and free-standing CF-NiCo₂O₄ composite.